Moist Thermodynamic Processes Leading to the Onset of Moist Tropical Heat Waves

Sofia A. Avila Nevarez

A Thesissubmitted in partial fulfillment of

the requirements for the degree of

Master of Science

(Atmospheric and Oceanic Sciences)

at the

University of Wisconsin-Madison

2026

Thesis Declaration and Approval

I, Sofia A. Avila Nevarez, declare that this Thesis titled 'Moist Thermodynamic Processes Leading to the Onset of Moist Tropical Heat Waves' and the work presented in it are my own.

Sofia A. Avila Nevarez		
Author	Signature	Date

I hereby approve and recommend for acceptance this work in partial fulfillment of the requirements for the degree of Master of Science:

Ángel F. Adames Corraliza		
Committee Chair	Signature	Date
Larissa E. Back		
Faculty Member	Signature	Date
Ankur Desai		
Faculty Member	Signature	Date

Abstract

Moist Thermodynamic Processes Leading to the Onset of Moist Tropical Heat Waves

by Sofia A. Avila Nevarez

The plume buoyancy framework used in previous work is applied to understand the processes that lead to moist tropical heat waves (HW). Lag composite analysis applied to land and ocean regions that often experience moist heat waves reveals that buoyancy is typically positive prior to the HW, becoming negative during HW onset due to an increase in saturation deficit, in agreement with previous work. The saturation deficit anomaly is mostly a result of warming in the lower free troposphere and drying at midlevels. It exhibits a nearly upright structure that extends from the surface to the upper troposphere. This structure motivates the use of a column saturation deficit budget to understand HW onset processes. It is found that subsidence driven by deviations from weak temperature gradient balance drives the increase in column saturation deficit, with horizontal moist static energy advection playing a smaller but non-negligible role.

Plain Language Summary

Moist tropical heat waves (HWs) are characterized by high surface temperature and humidity that can lead to heat stress and fatalities. Moist tropical HWs have received increased attention recently due to the risk they pose to human health. However, the processes that cause them are not fully understood. Previous work has shown that moist HWs develop as a result of drying of the air above the surface. Here, we focus on regions over land and ocean that often experience moist HWs, and find that the atmosphere is humid and cooler days prior to the HW but becomes drier and warmer at the onset. Further analysis shows a subsidence that is uncharacteristically strong for the tropics is largely responsible for the warming and drying.

Acknowledgements

I'd first like to thank my advisor, Ángel, for taking me in as a graduate student. These past few years have been insightful and challenging, yet fun. I greatly appreciate not only the depth he goes to understand our field, but the immense patience he has shown towards my learning. I fully believe no other advisor could have put up with me.

I would also like to thank Profs. Larissa Back and Ankur Desai for taking the time to read this thesis. I also greatly enjoyed the courses I took with them. I further extend my gratitude to all the educators in my life, who in one way or another have pushed me slightly in the direction I am now and for their patience in teaching me. I'd also like to thank Dr. Kimberly Hoogewind for introducing me to undergraduate research and encouraging me to pursue it further, and for also being the kindest scientist I know.

Of course, I have to thank my friends here at AOS: Idamis, Shane, and Ally. The first year was tough, but we made it through together. Thank you for listening, getting coffee with me, buying me little trinkets and legos, going to the gym with me and everything else. I love y'all.

I'd also like to thank my friends back home, Ruth and Brenda, who support my crazy dreams and keep me up to date with the shenanigans back home.

Finally, I'd like to thank my family: my sister, my brother, and especially my mother. Everything I do is for you.

Sofia <3

Contents

List of Figures

Chapter 1

Introduction

1.1 Moist Tropical Heat Waves

Heat waves (HWs) are persistent, anomalous periods of high surface temperatures that are reported to be one of the deadliest weather-related phenomena (Buzan and Huber, 2020). On average, over 500,000 fatalities occurred per year between 2000-2019 due to heat-related stress worldwide, many due to the impact of HWs Zhao et al. (2021). Heat stress can cause physiological responses such as dehydration and hyperthermia that can lead to death if untreated. Additionally, prolonged heat stress has been attributed to reduced labor productivity (De Sario et al., 2023) and decreased cognitive performance (Mazloumi et al., 2014). High humidity can further heat stress since it can reduce the capacity for humans to cool down through the evaporation of sweat (Buzan and Huber, 2020, Haldane, 1905). The compounded stress that high humidity imposes on the human body makes moist HWs — HWs that are accompanied by elevated surface humidity —particularly dangerous.

Much of the research on HWs has focused on midlatitude HWs characterized by high temperatures and low specific humidity, usually measured by the dry-bulb temperature (Kong and Huber, 2023, Raymond et al., 2017). The physical processes of these dry heat waves are relatively well understood. These dry midlatitude HWs are often characterized by large-scale subsidence due to a high-pressure system that leads to adiabatic warming (Pfahl and Wernli, 2012, Röthlisberger and Papritz, 2023) and are typically a part of a large-scale Rossby wave train pattern (Lembo et al., 2024). In contrast, moist HWs, which are commonly measured using the wet-bulb temperature (WBT), are not as well understood. Although moist HWs occur globally, the temporal co-occurrence of dry and moist heat extremes overlaps less in the subtropics and tropics, suggesting that moist HWs in these regions may be driven by different physical processes than dry HWs (Kong and Huber, 2023). To further complicate matters, studies show that as the climate warms, the tropics have the greatest increase in death risk associated with moist heat extremes in comparison to other regions (Mora et al., 2017). Thus, understanding the physics of this phenomena has become increasingly of interest.

1.2 Tropical Dynamics

1.2.1 Wet-Bulb Temperature and Moist Static Energy

Recent studies have adopted the use of the WBT to examine moist tropical HWs (Jackson et al., 2025, Zhang et al., 2021). WBT is the temperature an air parcel would have if cooled isobarically by evaporation. Its similarity to how the body cools by sweating makes WBT a useful metric to use for heat stress research. WBT is an enthalpy conserving variable, and can be used interchangeably with quasi-conserved variables such as the moist static energy (MSE; Raymond et al., 2017, see Appendix A for derivation). Zhang et al. (2021) hypothesized that surface WBT is constrained by the same atmospheric dynamics that constrain surface MSE, namely the weak temperature gradient approximation (WTG; Sobel et al., 2001) and convective quasi-equilibrium (QE; Emanuel et al., 1994).

1.2.2 Convective Quasi-Equilibrium and the Weak Temperature Gradient Approximation

Under QE (Emanuel et al., 1994), there is a balance between the large-scale environment pushing the atmosphere to larger boundary layer instability, which is balanced by a quick consumption of instability by deep convection. Under the QE formulation of Emanuel et al. (1994) – which we will refer to as conventional QE– the atmosphere is approximately neutrally buoyant to undilute parcels that rise moist adiabatically (i.e. they do not mix with environmental air). According to conventional QE, the surface moist static energy (MSE) and midtropospheric saturated MSE (MSE*) are equivalent in regions of undilute moist adiabatic ascent. Under WTG balance, the horizontal distribution of midtropospheric temperatures – and hence MSE*- are nearly uniform in the horizontal. Since HWs are characterized by neutral or negative buoyancy, it follows that regions that experience HWs should have a surface MSE* value that is equal to or less than the MSE of the convecting region (Duan et al., 2024).

However, the conventional QE-WTG framework tends to underestimate the WBTs observed during moist HWs since the surface MSE cannot persistently exceed the mid-troposphere MSE* (Duan et al., 2024, Zhang et al., 2021). The conventional form of QE frequently used by HW studies assumes that rising plumes in a convecting region are undilute. However, it is well-known that undilute updrafts are an uncommon occurrence in the tropics; most convection experiences extensive dilution (Brown and Zhang, 1997, Ferrier and Houze, 1989, Holloway and Neelin, 2009, Romps and Kuang, 2010, Zipser, 2003). If the environment is dry and the dilution is sufficiently strong, convection can be suppressed.

Through the inclusion of entrainment, Duan et al. (2024) developed an "entraining QE-WTG" framework that explains the thermodynamic conditions associated with moist tropical HWs. They found that moist HWs occur in dry environments where dilution is strong enough to suppress convection in spite of convective instability, allowing for the build-up of surface MSE. It is important to note that entraining-QE assumes a neutral entraining plume buoyancy, an assumption that breaks down at smaller (smaller than 0.25°) scales as seen using weather station data (Bowman and Back, 2025). According to (Bowman and Back, 2025), entraining-QE should be modified slightly to provide an upper limit to the surface WBT. The modification can be done by allowing a small, positive instability that can better represent the extremes captured by point scale measurements (Bowman and Back, 2025). Since our analysis uses reanalysis data and not point scale measurements, the buoyancy may be slightly underestimated, but this does not change the interpretation of the main results. Nevertheless, entraining-QE still serves as a conceptual framework as it provides a maximum surface surface WBT under the plume buoyancy framework (see Appendix B).

While the results of Duan et al. (2024) shed light into the conditions associated with moist HWs, the processes that lead to these conditions have not been carefully examined. In this study, we will employ a similar entraining plume framework as Duan et al. (2024) and relax the WTG and entraining quasi-equilibrium assumptions in order to examine the atmospheric processes associated with moist tropical HWs. Since updraft dilution is related to the saturation deficit of the troposphere, we will employ a "column saturation deficit" budget to examine the processes that lead to enhanced dilution. Our results show that the increase in the saturation deficit is due to anomalous subsidence that occurs during HW onset, which we conclude is due to deviations from WTG balance.

Chapter 2

Data and Methods

2.1 Data

The data used in this study comes from the fifth reanalysis from the European Centre for Medium-Range Weather Forecasts (ERA5 Hersbach et al., 2020). We make use of temperature (T), specific humidity (q), geopotential (Φ), and precipitation rate (P). All variables except P have 27 vertical levels from 1000-100 hPa. All fields have a $0.5° \times 0.5°$ latitude-longitude horizontal resolution and 6 hour time resolution. We also make use of P from the Tropical Rainfall Measurement Mission (TRMM Huffman et al., 2007) for the 18 year interval of 1998-2016. The TRMM data were provided at a 6-hourly, $0.5° \times 0.5°$ resolution. All of the four times daily data was averaged to create daily means.

2.2 Data Preparation

We first calculate the wet-bulb temperature (WBT) using daily means of q, T, and P following Davies-Jones (2008) and compute the 95th percentile (top 5%) of WBT from 25°S-25°N ($\sim$24.72 °C). We then find where this threshold is exceeded most often (Figure 2.1). We use 12 total regions that exhibit the largest fractional occurrence of moist

HWs as indicated by the boxes in Figure 1. Six of these grid boxes are considered predominantly 'land' regions (black boxes), while the remaining six grid boxes are considered predominantly 'ocean' regions (blue boxes).

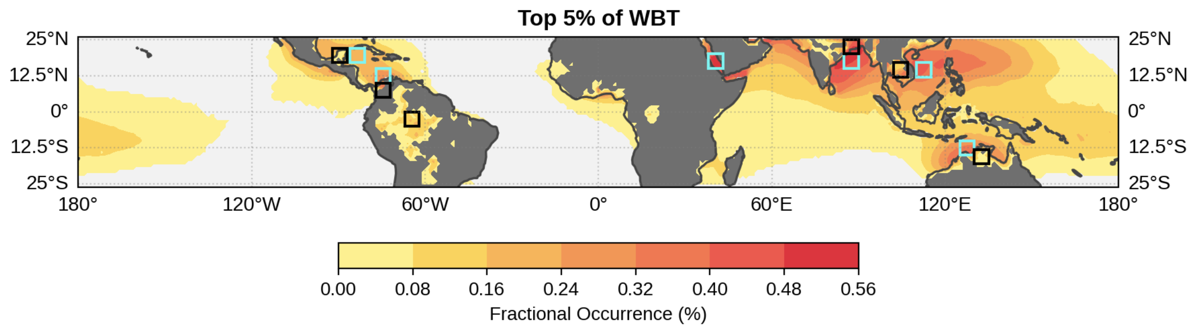

FIGURE 2.1: Fractional occurrence of the top 5% of wet-bulb temperature. The black boxes highlight the regions assessed in this study. Values less than 0.05 are ommitted

To isolate the signal of weather events that lead to tropical moist heat waves, we perform spectral analysis on daily WBT anomalies for each region. The anomalies are calculated by removing the time mean (1980-2018) from each grid cell, then removing the monthly mean (the seasonality). The power spectrum is computed using Welch's method (Welch, 1967), which involves dividing the time record into overlapping 'segments' and averaging the periodogram of each segment to reduce the variance of the signal (Schmidt et al., 2019), similar to multi-taper methods that have been used to evaluate periodicity of weather/climate regimes (e.g., Hartmann and Michelsen, 1989, Thompson and Barnes, 2014). Our segments overlap by 50% and are tapered using a Hann window with a length of 365 days to reduce spectral leakage, and each segment also has a length of 365 days.

The statistical significance of the spectral peaks are found by computing the red noise ('null hypothesis') of each spectra followed by the red noise and original spectra variances. The ratio of these two variances gives the F-statistic, and if the difference between the original spectra and the F-statistic exceeds the 99% significance level, then it is considered statistically significant. In most regions, a statistically-significant signal is found at timescales ranging from 5 to 40 days. Hence, we will apply a bandpass filter of 5-40 days to all variables used in this study.

2.2.1 Buoyancy Calculation

Recent studies have employed a deep-inflow entraining plume model to incorporate the effects of environmental air on the plume buoyancy (Adames et al., 2021, Schiro et al., 2018). The deep-inflow entraining plume framework assumes a coherent-inflow mixing between the updraft and environmental air, which affects the convective system's buoyancy (Adames et al., 2021, Ahmed and Neelin, 2018, Schiro et al., 2018). Ahmed and Neelin (2018) and Adames et al. (2021) show that integrated buoyancy in the lower free troposphere (LFT) (B_L) is highly correlated with precipitation over land and ocean. Buoyancy may also be useful in understanding the processes that can lead to suppressed convection (Duan et al., 2024) since negative B_L implies a non-convective environment. In our definition of buoyancy, we will follow Ahmed and Neelin (2018) and Adames et al. (2021) and decompose the buoyancy into surface-based instability and saturation deficit components as follows:

$$B_L = \frac{g}{\kappa_L C_p T_L}[w_B(h_{2m} - h_L^*) - w_L L_v(q_L^* - q_L)] \tag{2.1}$$

Subscripts B and L denote the boundary-layer and LFT layer, respectively, and superscript * denotes a saturated quantity. L_v is the latent heat of vaporization, C_p is the specific heat capacity of dry air at constant pressure, g is the gravitational acceleration, w_B and w_L are functions of the amount of mass-inflow and pressure thickness in each layer (Adames et al., 2021, Ahmed et al., 2020) with values of 0.3 and 0.7, respectively. The variable $\kappa = (1 + \frac{L_v^2 q^*}{C_p R_v T^2})$ scales the buoyancy by a factor of ~ 3 (Adames et al., 2021, Emmenegger et al., 2024), where R_v is the water vapor specific gas constant. MSE is defined as $h = C_pT + \Phi + L_v q$. The LFT layer average of a variable X is computed as $X_L = \frac{1}{950-600}\int_{950}^{600} X dp$. The boundary-layer average of a variable is computed as $X_B = \frac{1}{1000-950}\int_{1000}^{950} X dp$. We have defined the boundary layer to have a depth of 950hPa as in Vargas Martes et al. (2023), as this is the typical depth of the subcloud layer and where plumes typically originate from (Schiro and Neelin, 2019). We have also computed B_L using a depth of 850hPa and have found similar results.

2.2.2 Composites

We create a time series of WBT by calculating the spatial average of WBT from each of the regions in part a. We define a HW when the 95th percentile WBT is exceeded for at least 3 consecutive days. We do not merge HWs that occur close together in our analysis as we find that it does not noticeably change the overall number of events (not shown). The first day this threshold is exceeded is defined as the beginning of the heat wave and labeled as lag 'day 0'. Spatially-averaged composites of T, WBT, B_L, P, column MSE $\langle MSE \rangle$ and saturated column MSE $\langle MSE^* \rangle$ for each region are created for each lag day, starting at lag day -7 and ending at lag day 7. The brackets indicate a mass-weighted integration over the entire atmospheric column ($\langle X \rangle = \int_{100hPa}^{1000hPa} X dp/g$). We averaged the land and ocean regions highlighted in Figure 2.1 together to create land versus ocean composites for our assessment. For the purpose of presentation line composites have been smoothed using a cubic basis spline (B-spline), in which the points between each lag are interpolated to a finer grid consisting of 200 points.

Chapter 3

Results

3.1 Temperature, wet-bulb temperature and buoyancy

We begin by examining the spatially-averaged domains defined in Section 2 and use lag composite analysis. We first show 2m T, 2m WBT, and B_L anomalies starting at 7 days before the start of the HW, and ending 7 days after (Figure 3.1). The lags are defined in such a way that lag day 0 corresponds to HW onset. The temperature anomalies prior to day 0 in both composites are either slightly negative or approximately zero, and increase at the onset of the HW and peak around day 1-2, until around day 6 when the warm anomalies vanish. The positive T anomaly in the ocean composite is slightly lower than that of the land composite, likely due to WBT over the ocean having a larger moisture component. In both composites, the B_L anomalies follow an opposite pattern to the temperatures; B_L is positive prior to day 0 but decreases at the onset of the HW and becomes negative until day 6 when B_L becomes zero everywhere. These results are consistent with Duan et al. (2024).

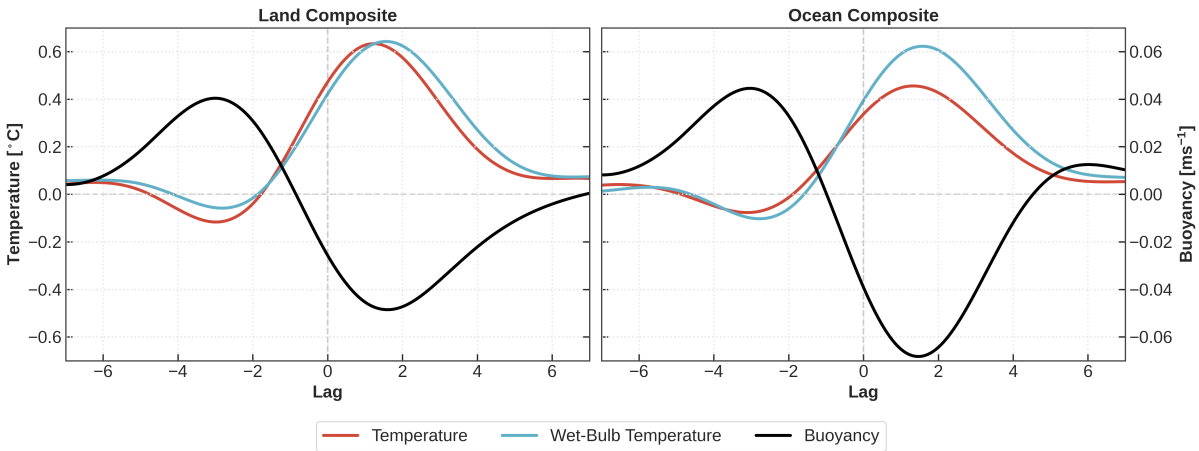

FIGURE 3.1: Land (left) and ocean (right) lag composites of 2-meter temperature (red), 2-meter wet-bulb temperature (blue) and buoyancy (black). Vertical gray dashed line highlights lag day 0, while the horizontal gray dashed line highlights the zero anomaly.

We further decompose B_L into surface-based instability and LFT saturation deficit components in Figure 3.2. The surface-based instability in both land and ocean composites does not vary much prior and after the HW onset, although the land composite does show a slightly stronger magnitude in this term at day 0. The LFT saturation deficit and B_L evolve similarly in both composites, suggesting that the LFT saturation deficit is largely responsible for the decrease in B_L at the onset of the HW when compared to the surface-based instability.

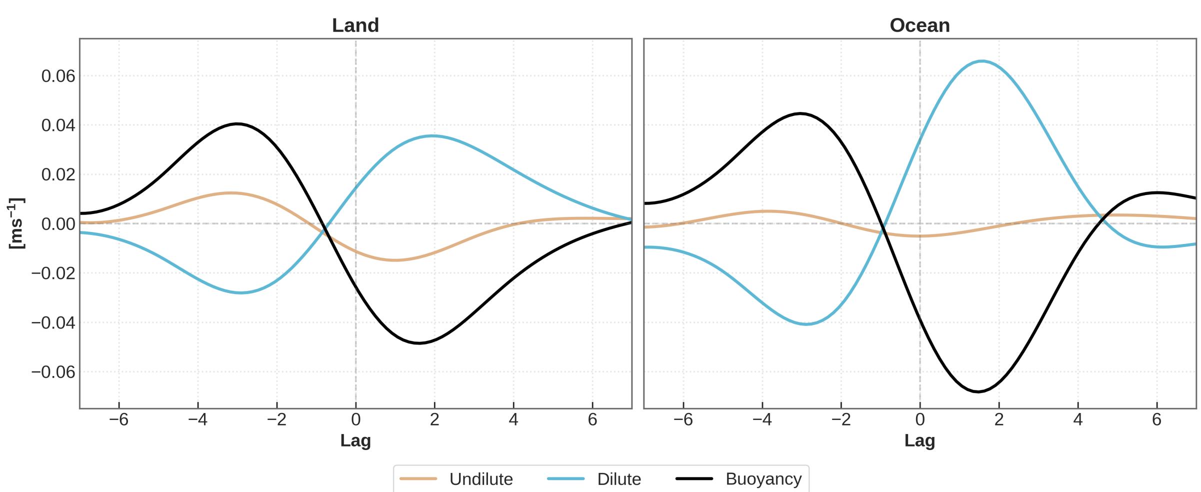

FIGURE 3.2: As in Figure 3.1 but for undilute/surface-based instability (orange), dilute/saturation deficit (blue) components of the buoyancy (black).

3.2 Moisture and Temperature Vertical Structure

In order to better understand the atmospheric conditions that lead to the reduction of B_L, we will now examine lag-pressure composites of q, T, ω, and the saturation deficit $q^* - q$ for land and ocean composites. Figure 3.3a and 3.3b show $q^* - q$ and ω anomalies 7 days before and after the start of the HW for pressure levels 1000-100 hPa, while Figure 3.3c and 3.3d shows T and q anomalies.

Over both land and ocean, there is a reduced saturation deficit ranging from 1000-400 hPa from days -6 to -2, accompanied by modest anomalous ascent that extends from 600 to 200 hPa (Figure 3.3a,b), and modestly enhanced q that ranges from 1000-400 hPa (Figure 3.3c,d). In Figure 3.4 we show that precipitation is enhanced at this time, particularly over ocean.

However, on day -1 deep tropospheric anomalous descent develops over both land and ocean (Figure 3.3a,b). The development of this descent coincides with drying and warming of the free troposphere as shown by the enhanced saturation deficit (Figure 3.3c,d). Although both land and ocean regions exhibit a similar development of the saturation deficit, the land regions exhibit a more pronounced warming in the mid and upper troposphere, while the oceanic regions exhibit more pronounced drying. In contrast, the boundary layer (1000-950 hPa) warms and moistens over both land and ocean. When considered together, we see a deep warming of the entire troposphere and a “dry over moist” pattern in anomalous moisture from lag day 0 to lag day 4. When the anomalous descent weakens we see that the free troposphere moistens and cools.

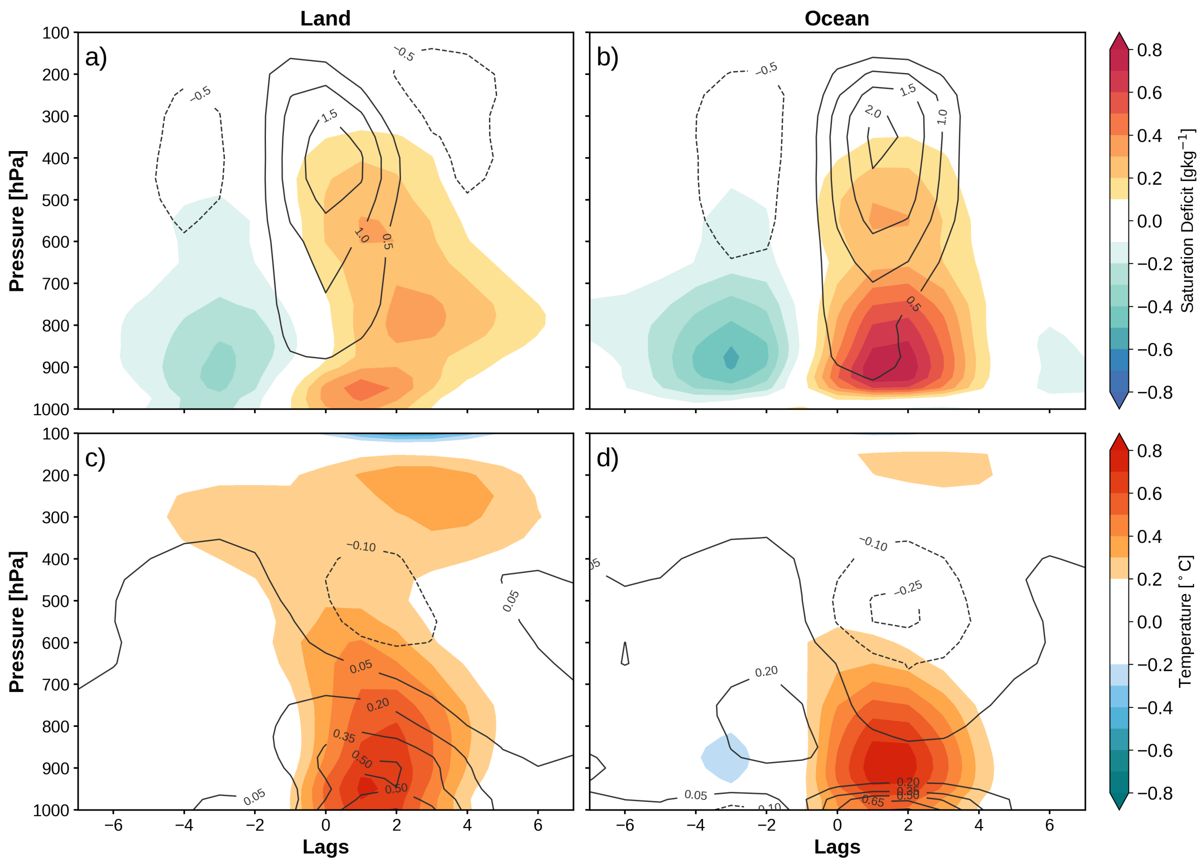

FIGURE 3.3: a) Lag-pressure land composite of the saturation deficit (shading) and omega (contours, units of Pa $s^{-1} \times 10^2$) anomalies. The red shading represents values where $q^* - q$ is stronger (further from saturation), while the blue shading represents values closer to saturation. The solid contour lines represent positive omega (downward motion) anomalies and the dashed lines represent negative omega (upward motion). b) as in panel a but for the ocean composite. c) as in panel a but for temperature (shading) and specific humidity (contours) anomalies. The red (blue) shading corresponds to warm (cool) anomalies. The solid contours lines are positive q (moist) anomalies whereas the dashed lines are negative q (dry) anomalies. d) as in c) but for the ocean composite. The shading and contours roughly correspond to statistically significant anomalies at the 99% significance level as determined by a two-tailed student's t-test (not shown)

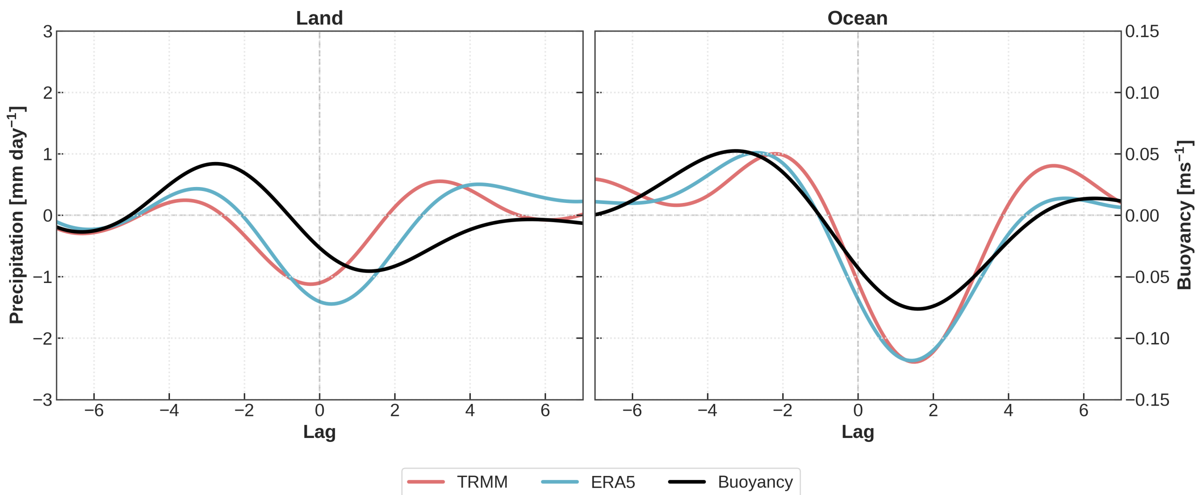

FIGURE 3.4: As in Figure 3.1 but for precipitation rate anomalies inferred from TRMM (red) and ERA5 (blue). Buoyancy is again shown in black. Note that because the TRMM product is only available for the years 1998-2016, the other two variables in these composites are also shown for that year range.

3.3 Column Saturation Deficit Budget

In Figure 3.2, we observed that an increase in the LFT saturation deficit $(q^* - q)$ is largely responsible for the reduction in B_L. In Fig. 3.3 we see that the processes occurring in the LFT are also occurring aloft. This is confirmed by computing the correlation coefficient between LFT $q^* - q$ and column-integrated $MSE^* - MSE$ over land and ocean composites, which show a relatively high correlation of about 66% and 70%, respectively (not shown). From here on, we will write $MSE^* - MSE$ as $\langle h^* - h \rangle$. Recall that $\langle h^* - h \rangle = \langle L_v(q^* - q) \rangle$. Due to this high correlation, we hypothesize that examining the processes that lead to changes in $\langle h^* - h \rangle$ may further elucidate the onset of moist HWs. Here, a positive value of $\langle h^* - h \rangle$ indicates enhanced column saturation deficit, whereas a negative value of $\langle h^* - h \rangle$ indicates a reduced column saturation deficit.

The processes that lead to changes in $\langle h^* - h \rangle$ can be understood by examining the "column saturation deficit budget", which we derive below:

3.3.1 Derivation of the Column Saturation Deficit Budget

We begin by defining the saturation deficit as $h^* - h$ where h is the moist static energy and h^* is the saturated moist static energy. To find how the $h^* - h$ evolves, it would first be convenient the express the moist static energy budget as:

$$\frac{Dh}{Dt} = Q_R - \frac{\partial \overline{\omega' h'}}{\partial p} \tag{3.1}$$

Where D/Dt is the material derivative, Q_R is the radiative heating and $\overline{w'h'}$ are the subgrid-scale fluxes of moist static energy. By expanding the left hand side of Eq.3.1 and column integrating, we have:

$$\frac{\partial \langle h \rangle}{\partial t} \simeq -\langle \mathbf{v} \cdot \nabla_h h \rangle - \left\langle \omega \frac{\partial h}{\partial p} \right\rangle + \langle Q_R \rangle + LFH + SFH \tag{3.2}$$

Where the LFH and SFH are the surface latent and sensible heat fluxes, respectively, and the angled brackets denote a mass-weighted integration from 100 to 1000 hPa. To find the saturation deficit budget, we must first find the expression for $\frac{Dh^*}{Dt}$. We may begin with the horizontal material derivative of the thermodynamic energy (enthalpy) equation:

$$\frac{D_h C_p T}{Dt} = -\omega \frac{\partial s}{\partial p} + Q_1 \tag{3.3}$$

Where T is temperature, s is the dry static energy, Q_1 is the apparent heating source, and C_p is the dry air constant at constant temperature. Following Adames (2022) we separate ω into its WTG and non-WTG term components: $\omega = \omega_Q + \omega_a$ where the subscripts Q and a represent the WTG and non-WTG component, respectively. Substituting this expression into Eq. 3.3:

$$\frac{D_h C_p T}{Dt} = -(\omega_Q + \omega_a) \frac{\partial s}{\partial p} + Q_1 \tag{3.4}$$

Under WTG balance, the apparent heating and vertical advection of dry static energy are in balance: $\omega_Q \frac{\partial s}{\partial p} = Q_1$ Adames (2022). By invoking WTG, Eq. 3.4 becomes:

$$\frac{D_h C_p T}{Dt} = -\omega_a \frac{\partial s}{\partial p} \tag{3.5}$$

Following (Adames et al., 2021, see their Appendix A), we can make the following approximate relationship between h^* and T:

$$C_p dT \simeq \frac{dh^*}{\kappa} \tag{3.6}$$

Where $\kappa = (1 + \frac{L_v^2 q^*}{C_p R_v T^2})$ scales the buoyancy by a factor of ~ 3 (Adames et al., 2021, Emmenegger et al., 2024), q^* is the saturated specific humidity, R_v is the water vapor specific gas constant, and L_v is the latent heat of vaporization. Following this relationship, we can rewrite Eq. 3.6 as:

$$\frac{D_h C_p T}{Dt} \simeq \frac{1}{\kappa} \frac{D_h h^*}{Dt} \tag{3.7}$$

We can substitute Eq. 3.7 into Eq. 3.5

$$\frac{1}{\kappa}\frac{D_h h^*}{Dt} \simeq -\omega_a \frac{\partial s}{\partial p} \tag{3.8}$$

Expanding yields:

$$\frac{\partial h^*}{\partial t} \simeq NW \tag{3.9}$$

where

$$NW \equiv -\left(\mathbf{v}\cdot\nabla_h h^* + \kappa\omega_a \frac{\partial s}{\partial p}\right) \tag{3.10}$$

is the non-WTG term.

By column-integrating 3.10 and subtracting Eq. 3.2, we obtain the following:

$$\frac{\partial}{\partial t}\langle h^* - h\rangle \simeq \langle \mathbf{v}\cdot\nabla_h h\rangle + \left\langle \omega\frac{\partial h}{\partial p}\right\rangle - \langle Q_R\rangle - SFH - LFH + NW \tag{3.11}$$

We can simplify Eq. 3.11 by defining the column process as $C = \langle \omega \frac{\partial h}{\partial p}\rangle - \langle Q_R\rangle - SFH - LHF$, so that the saturation deficit budget becomes:

$$\frac{\partial}{\partial t}\langle h^* - h\rangle \simeq \langle \mathbf{v}\cdot\nabla_h h\rangle - C + NW \tag{3.12}$$

The terms from left to right are the tendency of column saturation deficit, the horizontal advection of MSE, the column process, which combines latent heat fluxes, sensible heat fluxes, radiative heating, and the vertical advection of MSE (Chikira, 2014). The last term corresponds to changes in h^* due to warming and cooling driven by deviations from WTG balance which we will refer to as the non-WTG term for short. The sign convention of NW is so that a positive value corresponds to warming of the column, whereas a negative value corresponds to a cooling of the column. The brackets indicate a mass-weighted integration over the entire atmospheric column. The interpretation of the NW term will be given in the following subsection.

3.3.2 Non-WTG Warming

To first order, horizontal temperature and pressure gradients are not sustained in the tropical atmosphere. We can assume that an isobaric surface is roughly equivalent to an isentropic surface in the tropics, given that both surfaces are horizontally flat and mostly vary in the vertical.

A property of isentropic surfaces is that in the presence of diabatic heating, the isentropic surface does not vary in the vertical, such that the properties bounded by two isentropic surfaces remain constant. In the tropics, this would correspond to the maintenance of WTG balance even in the presence of diabatic heating Adames (2022). On the other hand, a motion strong enough to vary the isentropic surface such that they 'stretch' or 'compress' would be considered a deviation from WTG balance Adames (2022). An illustration is given in Figure 3.5.

Following this, we may interpret the NW term in Equation 3.12 as an 'isentropic warming' term, such that a positive deviation from WTG balance induces isentropic compression that warms the atmospheric column.

3.3.3 Lag Composites of Budget Terms

We show the column-integrated saturation deficit budget terms in Figure 3.6. The term in the budget that contributes the most is the non-WTG term, which explains up to 93% and 95% of the total tendency variance (correlation squared) in land and ocean composites, respectively (not shown). Both composites exhibit strong non-WTG warming prior to the onset near lag day -1. The tendency is also positive, suggesting that deviations from WTG drive the descent, warming the column and therefore enhancing the column saturation deficit (Figure 3.3a,b). The non-WTG anomaly exceeds the magnitude of the tendency anomaly over land on lag day -1. Near lag day 2, the term becomes negative over land and ocean, indicating that the column is cooling and the HW weakening. In contrast to the tendency and non-WTG term, the horizontal advection of MSE is weaker in amplitude over land and ocean, contributing to less than 30% and 1% to the total

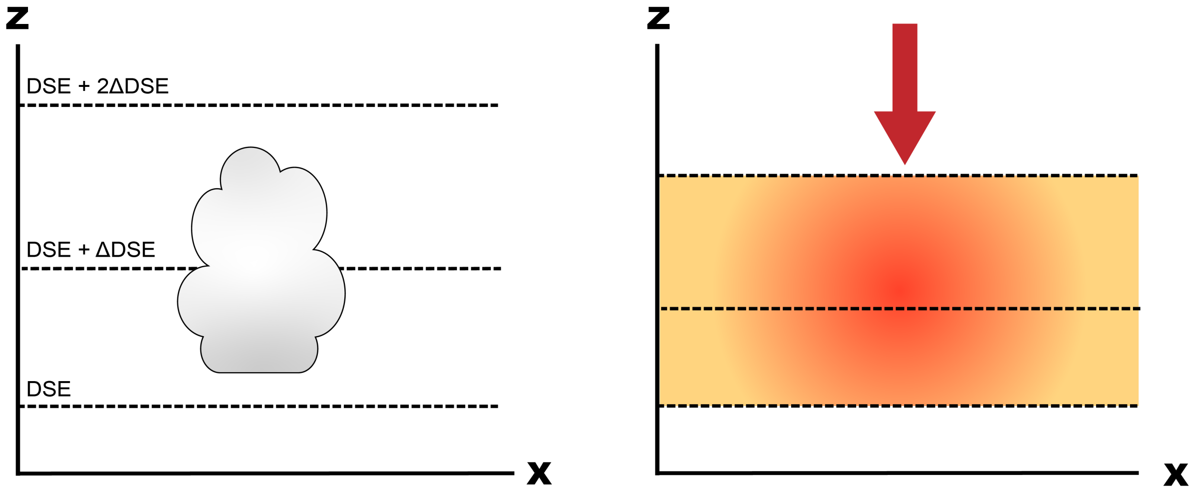

FIGURE 3.5: An idealized schematic representing the consequence of diabatic heating on the isentropic surfaces in the left panel, and a vertical motion induced by a deviation from weak temperature gradient balance. The gray dashed lines represent lines of constant dry static energy, and the cloud represents a source of diabatic heating. The red arrow on the right panel corresponds to a vertical motion induced by non-WTG motions, and the red shading represents the increase of temperature by the isentropic compression.

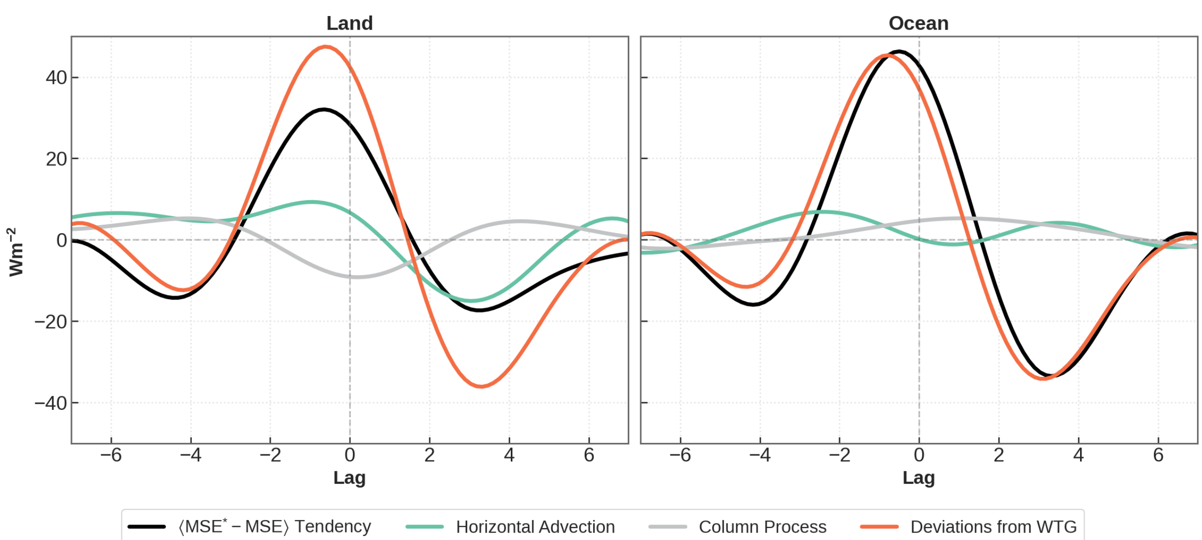

FIGURE 3.6: Lag composites of the terms in the column saturation budget equation: the column saturation deficit tendency (black), horizontal advection of moist static energy (teal), column process (gray), and deviations from weak temperature gradient balance (orange). The vertical gray dashed line highlights lag day 0, whereas the horizontal gray dashed line highlights the zero anomaly.

tendency variance, respectively. The horizontal advection of MSE is slightly positive prior to and at the onset of the HW, and becomes negative after. Overall, the initial moistening of the column in Figure 3.3c,d may be explained by the positive anomalous horizontal MSE advection. Over both land and ocean, the column process plays a smaller role than both the horizontal advection of MSE and non-WTG term.

Chapter 4

Conclusions

In this study, we aimed to examine the processes that lead to the onset of moist tropical HWs. We found that the processes responsible for moist tropical HWs are simlar over land and ocean, and are summarized in Figure 4.1. We found that a decrease in entraining plume buoyancy (B_L) coincides with HW onset over land and ocean (Figure 3.1). Free tropospheric saturation deficit plays a governing role in this decrease (Figure 3.2), in agreement with Duan et al. (2024). Prior to the onset, we noted a positive B_L anomaly and anomalous ascent accompanied by a moist column (Figure 3.3b). Anomalous precipitation is found to occur prior to the HWs (Figure 3.4) and is shown as a cloud in Figure 4.1. Non-WTG anomalous descent occurs around lag day -1 (shown as a purple arrow in Figure 4.1), which warms the troposphere and coincides with HW onset. The q^* increases as a result of the warming, thus increasing the saturation deficit and reducing B_L. During this time, the boundary layer becomes anomalously moist, as shown by the blue shading in Figure 4.1. The anomalous descent and enhanced saturation deficit aloft help maintain the moist boundary layer anomaly by suppressing convection. The suppressed rainfall at the onset is consistent with some previous work (Duan et al., 2024).

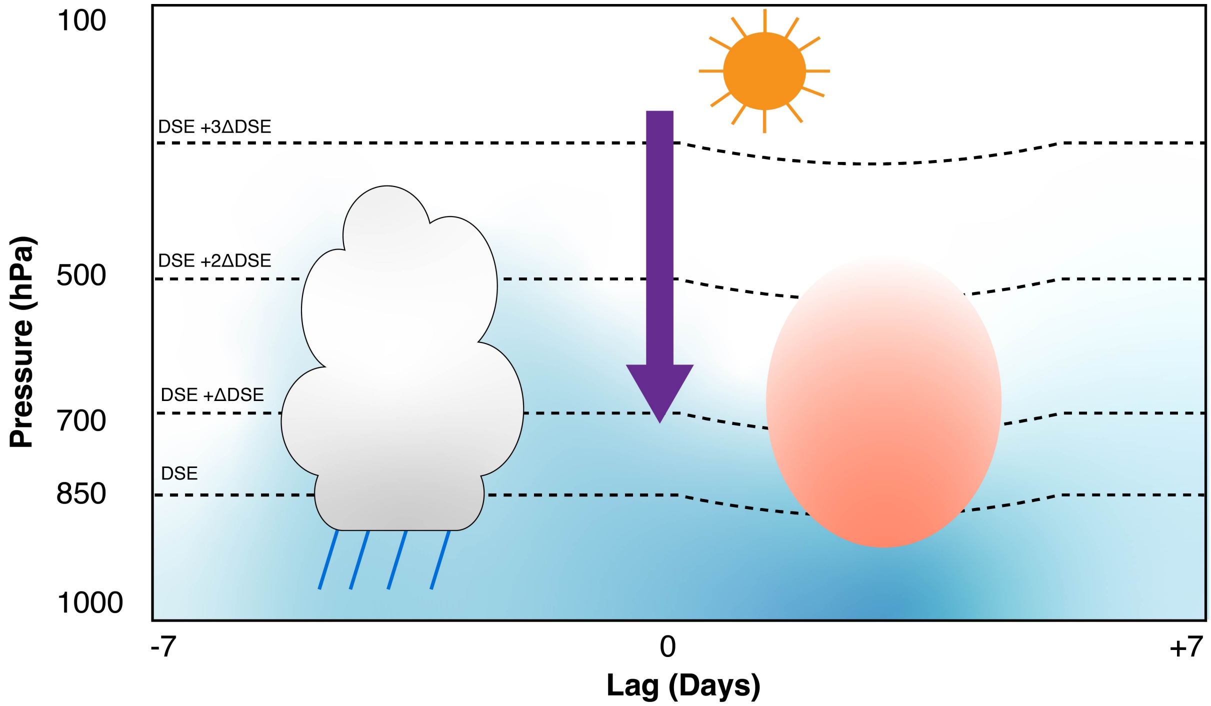

FIGURE 4.1: Schematic summarizing key points of result with lag days along the x-axis and the pressure along the y-axis. The dotted lines represent isentropes (lines of constant dry static energy), the red shading represent positive temperature anomalies, the blue shading represents positive moisture anomalies, and the purple arrow denotes non-WTG subsidence.

While the tropical atmosphere largely obeys the WTG approximation, we found that small deviations from this balance largely account for HW onset. It is noteworthy that the temperature anomalies themselves are not large, on the order of 1K or less, and do not substantially change the moist stability of the atmosphere (Figure 3.3c,d). In spite of their smallness, the temperature anomalies modulate the saturation specific humidity enough to account for most of the enhanced saturation deficit that ultimately suppresses convection. According to the results of Duan et al. (2024), increased saturation deficit near 850 hPa helps maintain a negative buoyancy when surface MSE exceeds the mid-troposphere MSE* and largely explains moist HW occurrence. Our results extends upon their work by showing that the saturation deficit is not only higher near the surface, but extends to the upper troposphere, and that its increase is largely a result of warming, with drying playing a secondary role.

While this study sheds some light onto the processes that lead to HW onset, several unanswered questions remain. For example, the fact that the column saturation deficit increases over a deep layer of the troposphere indicates that large-scale dynamics play an important role in moist HW onset. Scale analysis of tropical motions (e.g. Adames, 2022, Sobel et al., 2001, Yano and Bonazzola, 2009) suggests that motions that could create large deviations from WTG balance must be larger in scale than the Rossby deformation radius. This scaling limits the types of motions that could create moist HWs to planetary scale systems such as Rossby waves. This would make the mechanisms leading to moist tropical HWs similar to those of midlatitude HWs. However, more work is needed to better characterize the large-scale dynamics that lead to HW onset. Another unanswered question relates to the buildup of MSE near the surface. It is still worthwhile to examine the MSE budget of the BL to better understand the increase in WBT. Furthermore, it should be noted that the spatial scale resolution used in this study may not account for subgrid scale phenomena that can also modulate the boundary layer MSE, or that may contribute to the horizontal advection of MSE. For example, this can include mesoscale circulations that can moisten the boundary layer and modulate the near-surface MSE. Lastly, we noted that convection is often present prior to the onset of moist HWs, but we have not examined whether pre-existing convection plays a role in the HW, such as moistening the boundary layer. All these questions could be potentially fruitful directions for future research.

Appendix A

Derivation of the wet-bulb temperature

In this section, we show that the near-surface moist static energy (h) and the wet-bulb temperature (T_w) are physically related. We begin with the thermodynamic energy equation (1st law of thermodynamics) in its total differential form:

$$C_p dT = dQ + \alpha dp \tag{A.1}$$

where C_p is the specific heat capacity at constant pressure, dQ is the heat input , α is the specific volume, and p is the pressure. For the purpose of illustration, we take the derivatives to correspond to total time derivatives (i.e. $dT = dT/dt$). Following this definition, dQ is the diabatic heating rate, and here it is equal to $dQ = -L_v(c-e)$ where L_v is the latent heat of vaporization, and c and e are the condensation and evaporation rates, respectively. Additionally, we invoke hydrostatic balance $-\alpha dp \approx gdz$, where g is the gravitational acceleration and z is the height. Assuming that diabatic heating comes from evaporation and condensation, we have that $dQ = -L_v dq$, where q is the specific humidity. With these assumptions, we rewrite Equation A.1 as:

$$dh = C_p dT + L_v dq + g dz. \tag{A.2}$$

Since T_w is defined as the temperature at which an air parcel cools at constant pressure ($dp = 0$) through evaporation ($dQ \simeq -L_v e$) until reaching saturation, we may integrate Equation A.1 as:

$$\int_T^{T_w} C_p dT = -\int_q^{q^*(T_w)} L_v dq \tag{A.3}$$

where q_w^* is the saturared specific humidity at the wet-bulb temperature. Following this, we can write an expression for T_w as:

$$C_p T + L_v q = C_p T_w + L_v q^*(T_w) \tag{A.4}$$

Note that the left hand side of Equation A.5 is equal to the MSE near the surface, where $z \approx 0$. Using the Clausius-Clapeyron equation, we can show that

$$dh = \kappa C_p dT_w \tag{A.5}$$

where $\kappa = (1 + \frac{L_v^2 q^*(T_w)}{C_p R_v T_w^2})$. Thus, h and T_w are physically equivalent in that they follow the same conservation principles near the surface.

We show their relationship in Figure A.1, which illustrates a strong linear relationship between 2m T_w and 2m MSE.

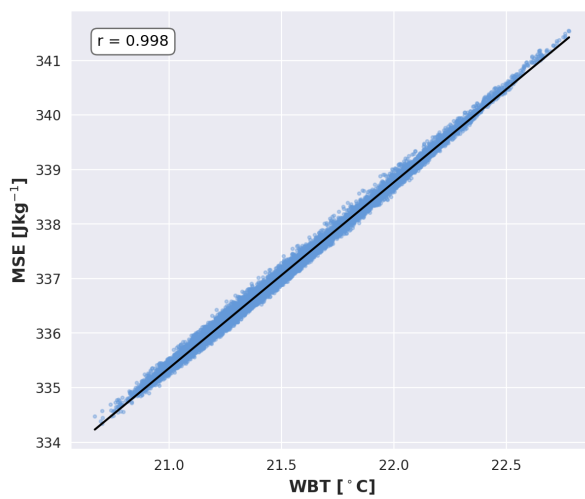

FIGURE A.1: Scatterplot between the 2-meter wet-bulb temperature and the near surface moist static energy averaged between 20S-20N using reanalysis data from ERA5. The correlation coefficient is located at the top left of the panel.

Appendix B

Surface wet bulb temperature in the buoyancy framework

We can rearrange the terms in Equation 1 of the main text to obtain the following expression for the surface MSE:

$$h_{2m} = h_L^* + \frac{w_L}{w_B} L_v (q_L^* - q_L) - h^- \tag{B.1}$$

where $h^- = -\kappa_L C_p T_L B_L / (w_B g)$. The surface WBT can be diagnosed by using Equations B.1 and Eq. A.4. Under conventional QE, the second and third terms on the right-hand side are 0 and hence the surface wet-bulb temperature is constrained by h^*. Considering the effects of dilution allows for higher surface wet-bulb temperatures, as the second term on the right-hand side of Eq. B.1 is always positive. This is the premise behind entraining quasi-equilibrium. If $B_L < 0$ the third term will diminish the WBT. Hence, entraining QE gives the maximum surface WBT that is possible under the plume buoyancy framework. An inspection of this term for the composites shown in Fig. 2 reveals that surface WBTs are a few Kelvin lower than expected from a strict application of entraining QE.

Bibliography

Adames, F., 2022: The Basic Equations under Weak Temperature Gradient Balance: Formulation, Scaling, and Types of Convectively Coupled Motions. *Journal of the Atmospheric Sciences*, **79**, 2087–2108, doi:10.1175/JAS-D-21-0215.1.
URL `https://journals.ametsoc.org/view/journals/atsc/79/8/JAS-D-21-0215.1.xml`

Adames, F., S. W. Powell, F. Ahmed, V. C. Mayta, and J. D. Neelin, 2021: Tropical Precipitation Evolution in a Buoyancy-Budget Framework. *Journal of the Atmospheric Sciences*, **78**, 509–528, doi:10.1175/JAS-D-20-0074.1.
URL `https://journals.ametsoc.org/view/journals/atsc/78/2/jas-d-20-0074.1.xml`

Ahmed, F., F. Adames, and J. D. Neelin, 2020: Deep Convective Adjustment of Temperature and Moisture. *Journal of the Atmospheric Sciences*, **77**, 2163–2186, doi:10.1175/JAS-D-19-0227.1.
URL `https://journals.ametsoc.org/view/journals/atsc/77/6/JAS-D-19-0227.1.xml`

Ahmed, F. and J. D. Neelin, 2018: Reverse Engineering the Tropical Precipitation–Buoyancy Relationship. *Journal of the Atmospheric Sciences*, **75**, 1587–1608, doi:10.1175/JAS-D-17-0333.1.
URL `https://journals.ametsoc.org/doi/10.1175/JAS-D-17-0333.1`

Bowman, Q. and L. Back, 2025: Tropical moist heat extremes on small scales are not well constrained by reanalysis-derived quasi-equilibrium relationships. *Geophysical Research Letters*, **52**, e2025GL117372, doi:https://doi.org/10.1029/2025GL117372, e2025GL117372 2025GL117372.
URL `https://agupubs.onlinelibrary.wiley.com/doi/abs/10.1029/2025GL117372`

Brown, R. G. and C. Zhang, 1997: Variability of Midtropospheric Moisture and Its Effect on Cloud-Top Height Distribution during TOGA COARE*. *Journal of the Atmospheric Sciences*, **54**, 2760–2774, doi:10.1175/1520-0469(1997)054¡2760:VOMMAI¿2.0.CO;2.
URL `http://journals.ametsoc.org/doi/10.1175/1520-0469(1997)054<2760:VOMMAI>2.0.CO;2`

Buzan, J. R. and M. Huber, 2020: Moist Heat Stress on a Hotter Earth. *Annual Review of Earth and Planetary Sciences*, **48**, 623–655, doi:10.1146/annurev-earth-053018-060100.
URL `https://www.annualreviews.org/doi/10.1146/annurev-earth-053018-060100`

Chikira, M., 2014: Eastward-Propagating Intraseasonal Oscillation Represented by Chikira–Sugiyama Cumulus Parameterization. Part II: Understanding Moisture Variation under Weak Temperature Gradient Balance. *Journal of the Atmospheric Sciences*, **71**, 615–639, doi:10.1175/JAS-D-13-038.1.
URL `https://journals.ametsoc.org/doi/10.1175/JAS-D-13-038.1`

Davies-Jones, R., 2008: An Efficient and Accurate Method for Computing the Wet-Bulb Temperature along Pseudoadiabats. *Monthly Weather Review*, **136**, 2764–2785, doi:10.1175/2007MWR2224.1.
URL `http://journals.ametsoc.org/doi/10.1175/2007MWR2224.1`

De Sario, M., F. K. de'Donato, M. Bonafede, A. Marinaccio, M. Levi, F. Ariani, M. Morabito, and P. Michelozzi, 2023: Occupational heat stress, heat-related effects and the related social and economic loss: a scoping literature review. *Frontiers in*

Public Health, **11**, 1173553, doi:10.3389/fpubh.2023.1173553.
URL `https://www.frontiersin.org/articles/10.3389/fpubh.2023.1173553/full`

Duan, S. Q., F. Ahmed, and J. D. Neelin, 2024: Moist heatwaves intensified by entrainment of dry air that limits deep convection. *Nature Geoscience*, **17**, 837–844, doi:10.1038/s41561-024-01498-y.
URL `https://www.nature.com/articles/s41561-024-01498-y`

Emanuel, K. A., J. David Neelin, and C. S. Bretherton, 1994: On large-scale circulations in convecting atmospheres. *Quarterly Journal of the Royal Meteorological Society*, **120**, 1111–1143, doi:10.1002/qj.49712051902.
URL `https://rmets.onlinelibrary.wiley.com/doi/10.1002/qj.49712051902`

Emmenegger, T., F. Ahmed, Y.-H. Kuo, S. Xie, C. Zhang, C. Tao, and J. D. Neelin, 2024: The Physics behind Precipitation Onset Bias in CMIP6 Models: The Pseudo-Entrainment Diagnostic and Trade-Offs between Lapse Rate and Humidity. *Journal of Climate*, **37**, 2013–2033, doi:10.1175/JCLI-D-23-0227.1.
URL `https://journals.ametsoc.org/view/journals/clim/37/6/JCLI-D-23-0227.1.xml`

Ferrier, B. S. and R. A. Houze, 1989: One-Dimensional Time-Dependent Modeling of GATE Cumulonimbus Convection. *Journal of the Atmospheric Sciences*, **46**, 330–352, doi:10.1175/1520-0469(1989)046¡0330:ODTDMO¿2.0.CO;2.
URL `http://journals.ametsoc.org/doi/10.1175/1520-0469(1989)046<0330:ODTDMO>2.0.CO;2`

Haldane, J. S., 1905: The Influence of High Air Temperatures No. I. *Epidemiology and Infection*, **5**, 494–513, doi:10.1017/S0022172400006811.
URL `https://www.cambridge.org/core/product/identifier/S0022172400006811/type/journal_article`

Hartmann, D. L. and M. L. Michelsen, 1989: Intraseasonal Periodicities in Indian Rainfall. *Journal of the Atmospheric Sciences*, **46**, 2838–2862, doi:10.1175/1520-0469(1989)046¡2838:IPIIR¿2.0.CO;2.
URL `http://journals.ametsoc.org/doi/10.1175/1520-0469(1989)046<2838:IPIIR>2.0.CO;2`

Hersbach, H., B. Bell, P. Berrisford, S. Hirahara, A. Horányi, J. Muñoz-Sabater, J. Nicolas, C. Peubey, R. Radu, D. Schepers, A. Simmons, C. Soci, S. Abdalla, X. Abellan, G. Balsamo, P. Bechtold, G. Biavati, J. Bidlot, M. Bonavita, G. De Chiara, P. Dahlgren, D. Dee, M. Diamantakis, R. Dragani, J. Flemming, R. Forbes, M. Fuentes, A. Geer, L. Haimberger, S. Healy, R. J. Hogan, E. Hólm, M. Janisková, S. Keeley, P. Laloyaux, P. Lopez, C. Lupu, G. Radnoti, P. De Rosnay, I. Rozum, F. Vamborg, S. Villaume, and J. Thépaut, 2020: The ERA5 global reanalysis. *Quarterly Journal of the Royal Meteorological Society*, **146**, 1999–2049, doi:10.1002/qj.3803.
URL `https://rmets.onlinelibrary.wiley.com/doi/10.1002/qj.3803`

Holloway, C. E. and J. D. Neelin, 2009: Moisture Vertical Structure, Column Water Vapor, and Tropical Deep Convection. *Journal of the Atmospheric Sciences*, **66**, 1665–1683, doi:10.1175/2008JAS2806.1.
URL `https://journals.ametsoc.org/doi/10.1175/2008JAS2806.1`

Huffman, G. J., D. T. Bolvin, E. J. Nelkin, D. B. Wolff, R. F. Adler, G. Gu, Y. Hong, K. P. Bowman, and E. F. Stocker, 2007: The TRMM Multisatellite Precipitation Analysis (TMPA): Quasi-Global, Multiyear, Combined-Sensor Precipitation Estimates at Fine Scales. *Journal of Hydrometeorology*, **8**, 38–55, doi:10.1175/JHM560.1.
URL `http://journals.ametsoc.org/doi/10.1175/JHM560.1`

Jackson, L. S., C. E. Birch, G. Chagnaud, J. H. Marsham, and C. M. Taylor, 2025: Daily rainfall variability controls humid heatwaves in the global tropics and subtropics. *Nature Communications*, **16**, 3461, doi:10.1038/s41467-025-58694-6.
URL `https://www.nature.com/articles/s41467-025-58694-6`

Kong, Q. and M. Huber, 2023: Regimes of Soil Moisture–Wet-Bulb Temperature Coupling with Relevance to Moist Heat Stress. *Journal of Climate*, **36**, 7925–7942, doi:10.1175/JCLI-D-23-0132.1.
URL `https://journals.ametsoc.org/view/journals/clim/36/22/JCLI-D-23-0132.1.xml`

Lembo, V., S. Bordoni, E. Bevacqua, D. I. V. Domeisen, C. L. E. Franzke, V. M. Galfi, C. I. Garfinkel, C. M. Grams, A. Hochman, R. Jha, K. Kornhuber, F. Kwasniok, V. Lucarini, G. Messori, D. Pappert, I. Perez-Fernandez, J. Riboldi, E. Russo, T. A. Shaw, I. Strigunova, F. Strnad, P. Yiou, and N. Zagar, 2024: Dynamics, Statistics, and Predictability of Rossby Waves, Heat Waves, and Spatially Compounding Extreme Events. *Bulletin of the American Meteorological Society*, **105**, E2283–E2293, doi:10.1175/BAMS-D-24-0145.1.
URL `https://journals.ametsoc.org/view/journals/bams/105/12/BAMS-D-24-0145.1.xml`

Mazloumi, A., F. Golbabaei, S. M. K. Mahmood Khani, Z. Kazemi, M. Hosseini, M. Abbasinia, and S. Farhang Dehghan, 2014: Evaluating Effects of Heat Stress on Cognitive Function among Workers in a Hot Industry. *Health Promotion Perspectives; EISSN 2228-6497*, doi:10.5681/HPP.2014.031.
URL `http://journals.tbzmed.ac.ir/HPP/Abstract/HPP_73_20141230161629`

Mora, C., B. Dousset, I. R. Caldwell, F. E. Powell, R. C. Geronimo, C. Bielecki, C. W. W. Counsell, B. S. Dietrich, E. T. Johnston, L. V. Louis, M. P. Lucas, M. M. McKenzie, A. G. Shea, H. Tseng, T. W. Giambelluca, L. R. Leon, E. Hawkins, and C. Trauernicht, 2017: Global risk of deadly heat. *Nature Climate Change*, **7**, 501–506, doi:10.1038/nclimate3322.
URL `https://www.nature.com/articles/nclimate3322`

Pfahl, S. and H. Wernli, 2012: Quantifying the relevance of atmospheric blocking for co-located temperature extremes in the Northern Hemisphere on (sub-)daily time scales.

Geophysical Research Letters, **39**, 2012GL052261, doi:10.1029/2012GL052261.
URL `https://agupubs.onlinelibrary.wiley.com/doi/10.1029/2012GL052261`

Raymond, C., D. Singh, and R. M. Horton, 2017: Spatiotemporal Patterns and Synoptics of Extreme Wet-Bulb Temperature in the Contiguous United States. *Journal of Geophysical Research: Atmospheres*, **122**, doi:10.1002/2017JD027140.
URL `https://agupubs.onlinelibrary.wiley.com/doi/10.1002/2017JD027140`

Romps, D. M. and Z. Kuang, 2010: Do Undiluted Convective Plumes Exist in the Upper Tropical Troposphere? *Journal of the Atmospheric Sciences*, **67**, 468–484, doi:10.1175/2009JAS3184.1.
URL `https://journals.ametsoc.org/doi/10.1175/2009JAS3184.1`

Röthlisberger, M. and L. Papritz, 2023: Quantifying the physical processes leading to atmospheric hot extremes at a global scale. *Nature Geoscience*, 210,216, doi:https://doi.org/10.1038/s41561-023-01126-1.

Schiro, K. A., F. Ahmed, S. E. Giangrande, and J. D. Neelin, 2018: GoAmazon2014/5 campaign points to deep-inflow approach to deep convection across scales. *Proceedings of the National Academy of Sciences*, **115**, 4577–4582, doi:10.1073/pnas.1719842115.
URL `https://pnas.org/doi/full/10.1073/pnas.1719842115`

Schiro, K. A. and J. D. Neelin, 2019: Deep convective organization, moisture vertical structure, and convective transition using deep-inflow mixing. *Journal of The Atmospheric Sciences*, **76**, 965,987, doi:https://doi.org/10.1175/JAS-D-18-0122.1.

Schmidt, O. T., G. Mengaldo, G. Balsamo, and N. P. Wedi, 2019: Spectral Empirical Orthogonal Function Analysis of Weather and Climate Data. *Monthly Weather Review*, **147**, 2979–2995, doi:10.1175/MWR-D-18-0337.1.
URL `http://journals.ametsoc.org/doi/10.1175/MWR-D-18-0337.1`

Sobel, A. H., J. Nilsson, and L. M. Polvani, 2001: The Weak Temperature Gradient Approximation and Balanced Tropical Moisture Waves*. *Journal of the Atmospheric*

Sciences, **58**, 3650–3665, doi:10.1175/1520-0469(2001)058¡3650:TWTGAA¿2.0.CO;2.
URL `http://journals.ametsoc.org/doi/10.1175/1520-0469(2001)058<3650:TWTGAA>2.0.CO;2`

Thompson, D. W. J. and E. A. Barnes, 2014: Periodic Variability in the Large-Scale Southern Hemisphere Atmospheric Circulation. *Science*, **343**, 641–645, doi:10.1126/science.1247660.
URL `https://www.science.org/doi/10.1126/science.1247660`

Vargas Martes, R. M., A. F. Adames Corraliza, and V. C. Mayta, 2023: The role of water vapor and temperature in the thermodynamics of tropical northeast pacific and african easterly waves. *Journal of The Atmospheric Sciences*, **80**, 2305,2322, doi:https://doi.org/10.1175/JAS-D-22-0177.1.

Welch, P., 1967: The use of fast Fourier transform for the estimation of power spectra: A method based on time averaging over short, modified periodograms. *IEEE Transactions on Audio and Electroacoustics*, **15**, 70–73, doi:10.1109/TAU.1967.1161901.
URL `http://ieeexplore.ieee.org/document/1161901/`

Yano, J.-I. and M. Bonazzola, 2009: Scale analysis for large-scale tropical atmospheric dynamics. *Journal of the atmospheric sciences*, **66**, 159–172.

Zhang, Y., I. Held, and S. Fueglistaler, 2021: Projections of tropical heat stress constrained by atmospheric dynamics. *Nature Geoscience*, **14**, 133–137, doi:10.1038/s41561-021-00695-3.
URL `https://www.nature.com/articles/s41561-021-00695-3`

Zhao, Q., Y. Guo, T. Ye, A. Gasparrini, S. Tong, A. Overcenco, A. Urban, A. Schneider, A. Entezari, A. M. Vicedo-Cabrera, A. Zanobetti, A. Analitis, A. Zeka, A. Tobias, B. Nunes, B. Alahmad, B. Armstrong, B. Forsberg, S.-C. Pan, C. Íñiguez, C. Ameling, C. De La Cruz Valencia, C. Åström, D. Houthuijs, D. V. Dung, D. Royé,

E. Indermitte, E. Lavigne, F. Mayvaneh, F. Acquaotta, F. de'Donato, F. Di Ruscio, F. Sera, G. Carrasco-Escobar, H. Kan, H. Orru, H. Kim, I.-H. Holobaca, J. Kyselý, J. Madureira, J. Schwartz, J. J. K. Jaakkola, K. Katsouyanni, M. Hurtado Diaz, M. S. Ragettli, M. Hashizume, M. Pascal, M. De Sousa Zanotti Stagliorio Coélho, N. Valdés Ortega, N. Ryti, N. Scovronick, P. Michelozzi, P. Matus Correa, P. Goodman, P. H. Nascimento Saldiva, R. Abrutzky, S. Osorio, S. Rao, S. Fratianni, T. N. Dang, V. Colistro, V. Huber, W. Lee, X. Seposo, Y. Honda, Y. L. Guo, M. L. Bell, and S. Li, 2021: Global, regional, and national burden of mortality associated with non-optimal ambient temperatures from 2000 to 2019: a three-stage modelling study. *The Lancet Planetary Health*, **5**, e415–e425, doi:10.1016/S2542-5196(21)00081-4. URL `https://linkinghub.elsevier.com/retrieve/pii/S2542519621000814`

Zipser, E. J., 2003: Some Views On "Hot Towers" after 50 Years of Tropical Field Programs and Two Years of TRMM Data. *Meteorological Monographs*, **29**, 49–49, doi:10.1175/0065-9401(2003)029¡0049:CSVOHT¿2.0.CO;2. URL `https://jounals.ametsoc.org/doi/10/1175/0065-9401(2003)029<0049:CSVOHT>2.0.CO;2`